

Supporting information

Understanding the Electrochemical Potential and Diffusivity of MnO/C Nanocomposites at Various Charge/discharge States

Chaofeng Liu¹, Haoyu Fu², Yanyan Pei¹, Jiandong Wu³, Vivek Pisharodi¹, Yang Hu¹,
Guohua Gao⁴, Robert J. Yang, Jihui Yang¹ and Guozhong Cao^{1*}

Experimental Section

Synthesis

10 mmol of KMnO₄ and 24 mmol of glucose were dissolved into 40 mL of DI water to form a brown solution. 20 mmol of MnCl₂ was dissolved into 30 mL of ethylene glycol to form a transparent orange solution at 60 °C. Then, the MnCl₂ solution was added into the mixture of KMnO₄ and glucose and rapidly stirred for 30 min. The precursor was transferred into a 100 mL Teflon lined stainless steel autoclave and treated at 180 °C for 6 h. The product was washed and centrifuged with DI water several times and dried at 60 °C in an oven overnight. Finally, the obtained powder was calcined with nitrogen gas at 500 °C at a heating rate of 5 °C/min for 2 h and then subsequently cooled at room temperature.

Structural Characterization

The crystalline structures and microstructures of samples were conducted using a X' Pert³ diffractometer (PANalytical, Netherlands) with a Cu-K α radiation source ($\lambda=1.54056$ Å) and a step size of 0.013°, as well as a cold field emission scanning electron microscope (FESEM, HITACHI SU8200) with the accelerating voltage of 5 kV and the working current of 10 μ A. The lattice image was observed through high-resolution transmission microscopy (HRTEM, FEI/Tecnai G2 F20 S-TWIN TMP) with an accelerating voltage of 200 kV. The Raman spectrum was collected at a resolution of 0.65 cm⁻¹ using a Horiba JOBIN YVON Raman system (LabRAM HR Evolution) and an argon ion laser (532 nm) as the excitation source. The total surface area was examined using nitrogen sorption analyses via a Micromeritics surface area and porosity analyzer (ASAP 2020 HD88, USA). The de-gassing condition was set to 250 °C for 4 h under a vacuum of 500 μ mHg (~0.67 mbar). All adsorption-desorption measurements were conducted at the temperature of the liquid nitrogen (-196 °C). The Barrett-Joyner-Halenda (BJH) method was adopted to calculate the mesopore surface area, pore volume and pore diameter, whereas the specific surface area and the pore volume of micropores were calculated using the t-method. A thermogravimetric analyzer/ differential scanning calorimetry (TGA/DSC) (Mettler-Toledo STAR^e system) was used to study the pyrolyzing reaction in the precursor with Ar gas flowing at a rate of 50 mL/min. The electrical conductivity of samples was measured using a direct current four-point probe technique (ST-2722 semiconductor resistivity of the powder tester, Suzhou Jingge Electronic. Co., Ltd.) at a pressure of 4 MPa.

Capacitor Fabrication and Electrochemical Characterization

The electrochemical performances of the samples were studied using 2032 coin cells. To prepare the working electrode, an aqueous slurry containing a mixture of active materials (MnO/C) and carboxymethyl cellulose (CMC) at a weight ratio of 90:10 was bladed onto Cu foil and then subjected to thermal treatment at 120 °C for 12 h in a vacuum. The mass loading of the active material on each electrode disk was 1.0-1.5 mg/cm². The electrolyte was 1 M LiPF₆ in a 1:1:1 (vol %) mixture of ethylene carbonate, dimethyl carbonate and diethyl carbonate, with a polypropylene film (Celgard 2400) separator. Li-ion capacitors were fabricated with activated carbon employed as the cathodes and MnO electrodes as the anodes. The specific surface area of the commercial activated carbon is approximately 1800 m²/g, as discovered in our previous work¹. The fabrication of cathodes is similar to the fabrication of anodes but instead uses Al foil. Half cells were also assembled and lithium foil was used as the counter electrode for investigating the electrochemical properties of the anode materials. All cells were assembled in an argon-filled glovebox in which both the oxygen and water content were below 1 ppm.

Galvanostatic charge-discharge tests were carried out on the coin cells using a Land CT2001A system (Wuhan, China) at various current densities. The operating voltage window for spindle MnO, activated carbon half cells, and Li-ion capacitors was 0.01-2.50 V (*vs.* Li/Li⁺), 2.00-4.50 V (*vs.* Li/Li⁺) and 0.10-4.00 V (MnO/C//AC), respectively. Cyclic voltammograms (CVs) were conducted using a Solartron SI 1287 at various sweeping rates to characterize the redox reactions of electrode materials during charge/discharge. Electrochemical impedance spectroscopy (EIS) was performed at 3.0 V using the Solartron 1287A in conjunction with a Solartron 1260A impedance analyzer over a frequency range of 100 kHz to 0.01 Hz and an AC amplitude of 10.0 mV. The current densities for the half cells were calculated based on the masses of the active material of the electrodes. The current densities of the Li-ion capacitors were calculated based on the total mass of the active materials of both electrodes. All electrochemical measurements were carried out at room temperature. The specific energy and specific power values of Li-ion capacitors were calculated as follows:

$$E = \int_0^{\Delta t} IV(t)dt = \int_0^C V(C)dC,$$

$$P = E/t,$$

where I is the applied current (A), V the charge/discharge voltage (V), C the total charge per unit weight (Ah/kg), and t the charge/discharge time (h). Additionally, the energy conversion efficiency is defined and calculated through the following equation,

$$\eta = \frac{E_{dis}}{E_{cha}} = \frac{\int_0^{C_{dis}} V(C)dC}{\int_0^{C_{cha}} V(C)dC} \times 100\%,$$

where E (Wh/kg), V (V), and C (Ah/kg) stand for energy density, voltage, and specific capacity, respectively.

Theoretical Calculations

The calculations were performed using the Vienna ab initio simulation package (VASP)² and the projector augmented wave pseudo potentials (PAW) approach,^{3, 4} along with the GGA-PBE exchange-correlation function.⁵ The electronic states were treated as valance electrons: Mn(3d⁶4s¹), O(2s²2p⁴), Li(2s¹), and the cutoff energy for the plane wave basis set was set to 500 eV, and the total energy converged to 10⁻⁵ eV. A k-points sampling of 11 × 11 × 11 was generated

automatically using the Monkhorst–Pack method. The single point energies were calculated using two different magnetic alignments: FM (ferromagnetic) and AFM (antiferromagnetic). Two calculations were performed to obtain the charge density of MnO and Mn and O atoms. After that, the software VESTA⁶ was used to obtain a map of the charge density difference. Based on the conversion reaction of MnO as described in equation (1), the open circuit voltage (OCV) was calculated by the change of free energy:

$$\text{OCV} = \frac{-\Delta G}{2F}$$

As the entropy and volume effect are negligible, ΔG is approximated by only the change of internal energy, and the OCV was calculated by the following equation:

$$\text{OCV} = \frac{U(\text{Li}_2\text{O}) + U(\text{Mn}) - U(\text{MnO}) - 2U(\text{Li})}{2F}$$

where F is the Faraday constant, and $E(\text{Li}_2\text{O})$, $E(\text{Mn})$, $E(\text{MnO})$ and $E(\text{Li})$ are the internal energy per mole of Li_2O , Mn, MnO and Li respectively.

Table S1. Lattice parameters of Li_2O , MnO, Li, FCC-Mn, Mn-BCC and LiMn

	a/Å	b/Å	c/Å	alpha/°	beta/°	gamma/°
Li_2O	4.634	4.634	4.634	90	90	90
MnO	4.445	4.445	4.445	90	90	90
Li	3.439	3.439	3.439	90	90	90
FCC-Mn	3.496	3.496	3.496	90	90	90
BCC-Mn	2.794	2.794	2.794	90	90	90
LiMn	4.509	4.509	4.509	90	90	90

(1) The voltage calculation on internal energies

The conversion reaction is $\text{MnO} + 2\text{Li}^+ + 2\text{e}^- \leftrightarrow \text{Mn} + \text{Li}_2\text{O}$ as shown in the main text.

Energy change in the reaction:

$$\Delta G_1 = E(\text{FCC-Mn}) + E(\text{Li}_2\text{O}) - E(\text{MnO}) - 2E(\text{Li}) = -8.900 - 14.313 - (-16.406) - 2*(-1.903) = -3.001 \text{ eV}$$

$$\text{OCV}_{\text{MnO}-1} = -\frac{\Delta G}{Fz} = \frac{3}{2} = 1.5 \text{ V} ,$$

$$\Delta G_2 = E(\text{BCC-Mn}) + E(\text{Li}_2\text{O}) - E(\text{MnO}) - 2E(\text{Li}) = -8.839 - 14.313 - (-16.406) - 2*(-1.903) = -2.940 \text{ eV}$$

$$\text{OCV}_{\text{MnO}-2} = -\frac{\Delta G}{Fz} = \frac{2.940}{2} = 1.47 \text{ V} ,$$

where F is Faraday constant and z is the number of transfer charges in the reaction.

(2) The formation energy of Li ion inserted MnO

If the inserted product is LiMnO and energy change is

$$\Delta E_1 = E(\text{LiMnO}) - E(\text{MnO}) - E(\text{Li}) = 2.50 \text{ eV} .$$

If the inserted product is Li_2MnO , the formation energy is

$$\Delta E_2 = E(\text{Li}_2\text{MnO}) - E(\text{MnO}) - 2E(\text{Li}) = 2.85 \text{ eV} .$$

The formation energies are positive, suggesting the products are difficult or impossible to form in the conversion process.

(3) The formation possibility of LiMn alloy after the conversion reaction, the formation energy is

$$\Delta E_3 = E(\text{LiMn}) - E(\text{Mn}) - E(\text{Li}) = -7.99 + 8.9 + 1.903 = 2.87 \text{ eV} .$$

It is impossible as the same reason mentioned above. Cubic MnO differs from MnS^7 and SnO_2^8 anodes, the latter will form intermediate or alloying phases in the electrochemical reaction.

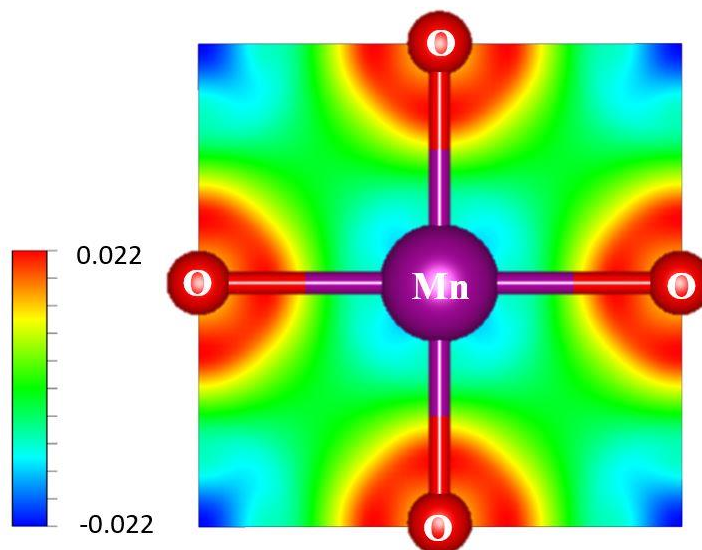


Figure S1. The charge density difference map of the Mn-O bond. No electron cloud overlapping occurs between them because the strong ionic bond makes the electrons tightly attracted to the anions.

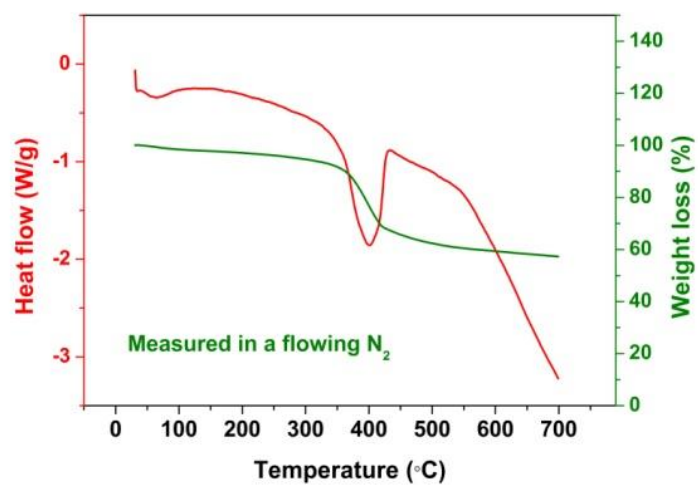


Figure S2. (a) DSC/TG curves of the solvothermal product tested with flowing nitrogen. The endothermal peak indicates the decomposition of MnCO_3 and the carbonization of aromatized glucose.

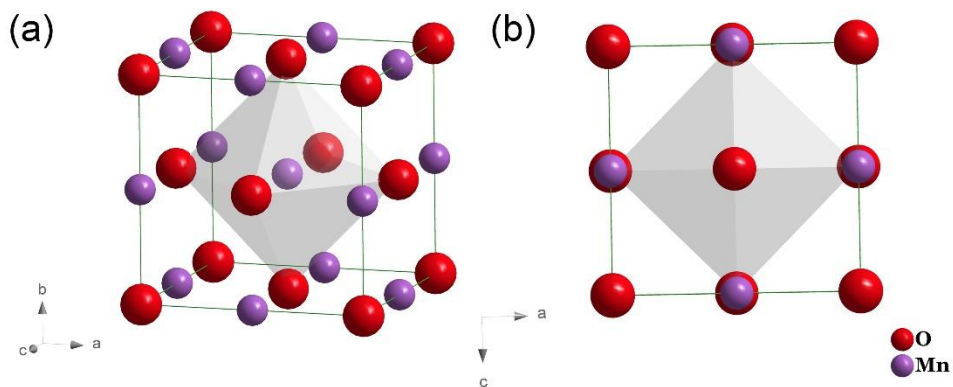


Figure S3. The rock-salt chemical structure of MnO .

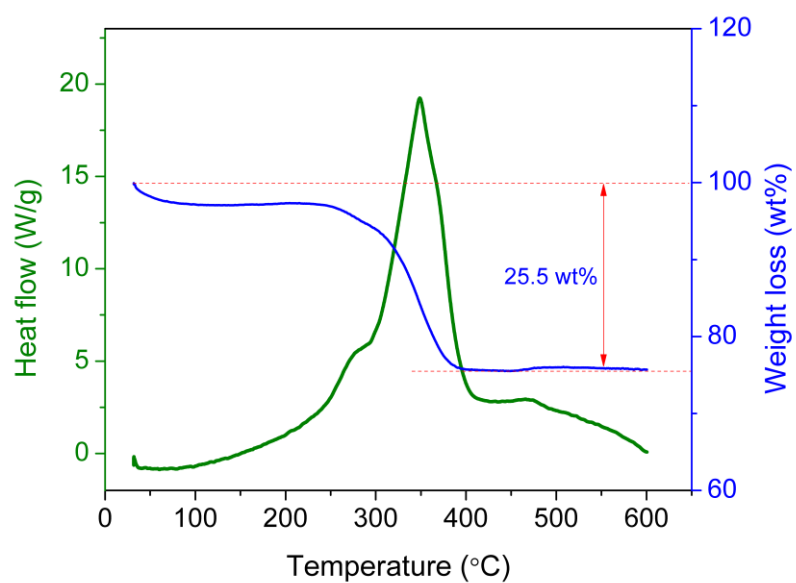


Figure S4. DSC/TG curves of the calcined sample tested with flowing oxygen. The exothermal peak at 350 °C implies the combustion of carbon.

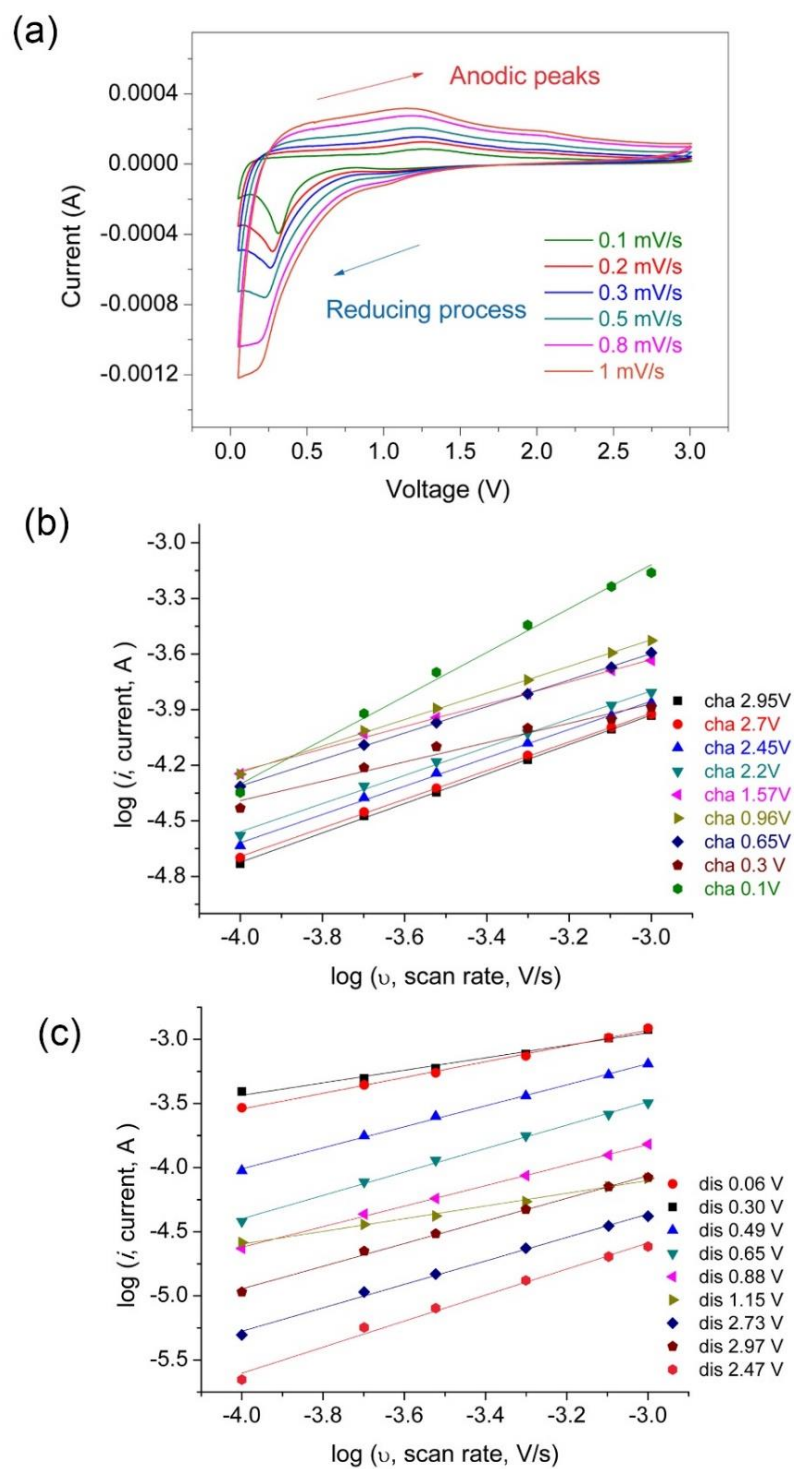


Figure S5. (a) CV curves at different sweeping rates. The relationship between $\log i$ and $\log v$ in the (b) charge and (c) discharge process.

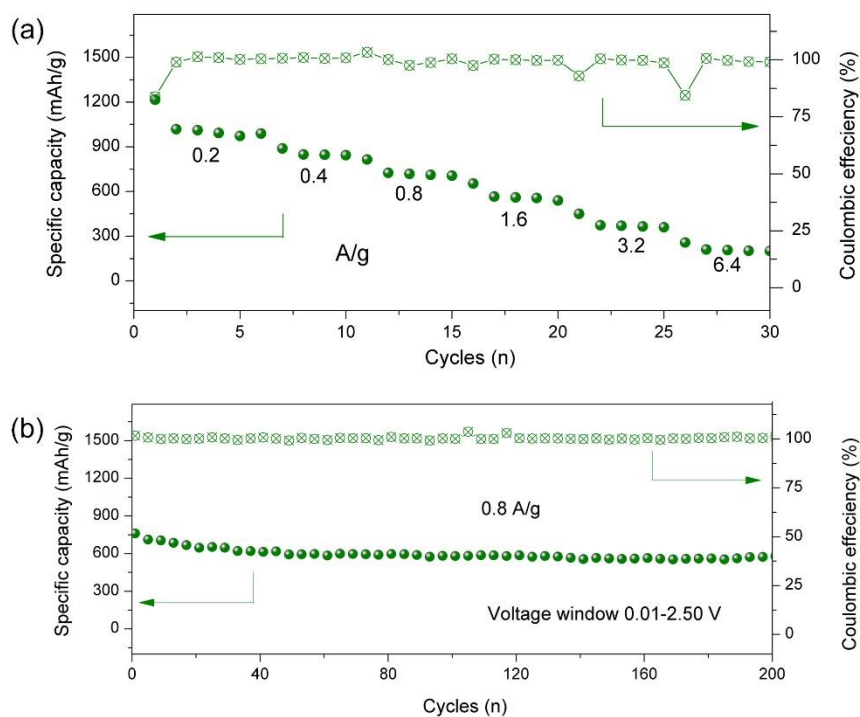
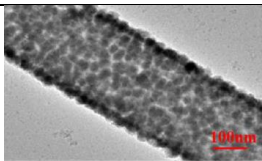
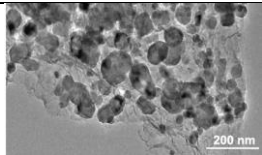
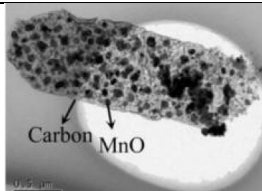
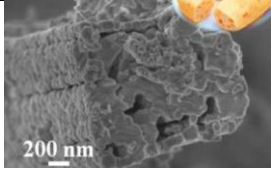
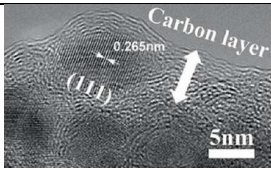
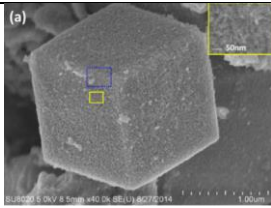
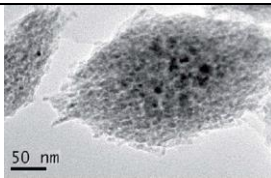
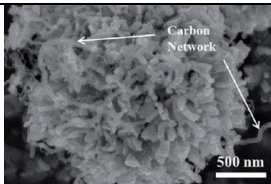
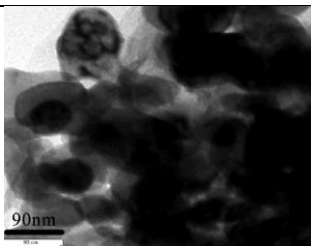
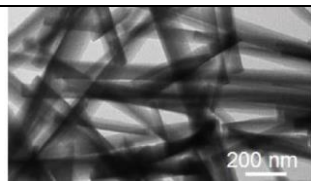
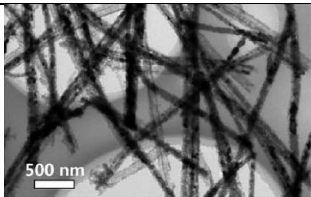
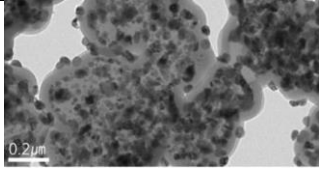
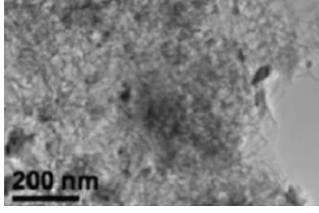
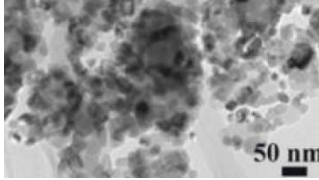

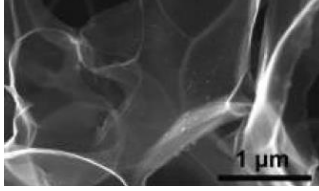
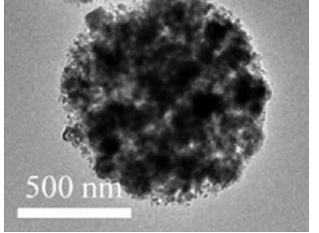
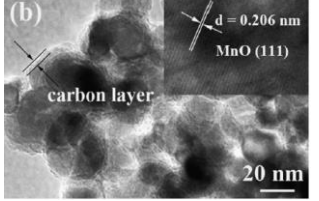


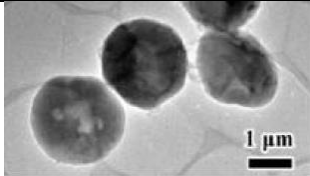
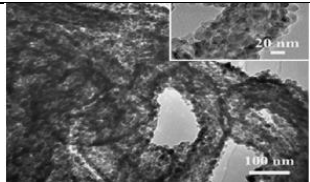
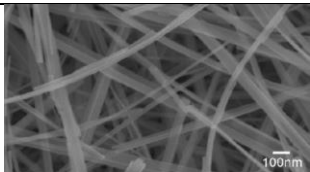
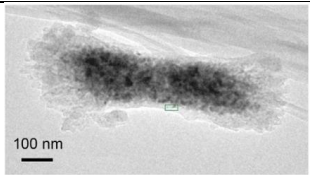
Figure S6 (a) Rate capability and (b) cycling stability of the MnO/C anode tested within the voltage window of 0.01-2.50 V. The capacity retention at a high current density remains excellent with no observed degradation appearing after 200 cycles.

Table S2. Comparison of MnO anodes for Li-ion batteries

Compositions	Morphologies	Specific capacity	Voltage window (V)	Refs.
MnO quantum dots embedded in carbon nanotubes		603 mAh g ⁻¹ over 100 cycles at 100 mA g ⁻¹	0.001-3.0	9
MnO nanosheets in densely stacked graphene		1000 mAh g ⁻¹ at 100 mA g ⁻¹	0.01-3.0	10
MnO/C Hybrids		800 mAh g ⁻¹ over 200 cycles at 1000 mA g ⁻¹	0.0-3.0	11

Lotus-Root-Like MnO/C Hybrids		695 mAh g ⁻¹ over 250 cycles at 1510 mA g ⁻¹	0.01-3.0	12
MnO/carbon		From 400 mAh g ⁻¹ to 1210.9 mAh g ⁻¹ over 700 cycles	0.005-3.0	13
Mesocrystal MnO cubes		637 mAh g ⁻¹ at 100 mA g ⁻¹	0.05-2.5	14
MnO/C nanoparticles		650 mAh g ⁻¹ at 1000 mA g ⁻¹ over 300 cycles	0.01-2.5	15
MnO/ double C		1077 mAh g ⁻¹ at 500 mA g ⁻¹ over 300 cycles	0.05-3.0	16
MnO/reduced graphite oxide composite		680 mAh g ⁻¹ at 500 mA g ⁻¹ over 300 cycles	0.01-3.0	17
MOF-derived ultrafine MnO nanocrystals		1221 mAh g ⁻¹ at 100 mA g ⁻¹ over 100 cycles	0.00-3.0	18
MnO/C coaxial nanowires		480 mAh g ⁻¹ at 1000 mA g ⁻¹ over 600 cycles	0.01-2.5	19

MnO/C nanocomposite		541 mAh g ⁻¹ at 100 mA g ⁻¹ over 100 cycles	0.01-3.0	20
MnO nanowire/graphene composite		860 mAh g ⁻¹ at 50 mA g ⁻¹	0.01-3.0	21
MnO /N-Doped Carbon		907 mAh g ⁻¹ at 5000 mA g ⁻¹ over 400 cycles	0.01-3.0	22
Peanut-like MnO@C		839 mAh g ⁻¹ at 200 mA g ⁻¹ over 200 cycles	0.01-3.0	23
MnO in Carbon Nanosheets		800 mAh g ⁻¹ at 2000 mA g ⁻¹ over 500 cycles	0.01-3.0	24
3D porous MnO/C microspheres		800 mAh g ⁻¹ at 200 mA g ⁻¹ over 100 cycles	0.01-3.0	25
Carbon-coated MnO		470 mAh g ⁻¹ at 100 mA g ⁻¹ over 100 cycles	0.01-3.0	26

Hollow Porous MnO/C Microspheres		702 mAh g ⁻¹ at 100 mA g ⁻¹ over 50 cycles	0.05-3.0	27
Nanoscaled MnO in N-doped carbon webs		From 650 mAh g ⁻¹ to 1268 mAh g ⁻¹ at 1000 mA g ⁻¹ over 700 cycles	0.01-3.0	28
MnO/C core-shell nanorods		620 mAh g ⁻¹ at 200 mA g ⁻¹ over 50 cycles	0.01-3.0	29
MnO/C		1018 mAh g ⁻¹ at 200 mA g ⁻¹ and 594 mAh g ⁻¹ at 800 mA g ⁻¹ over 200 cycles	0.01-2.5	This work

Note: The work voltage window affects the specific capacity, thus the special comparison should be under the same testing conditions.

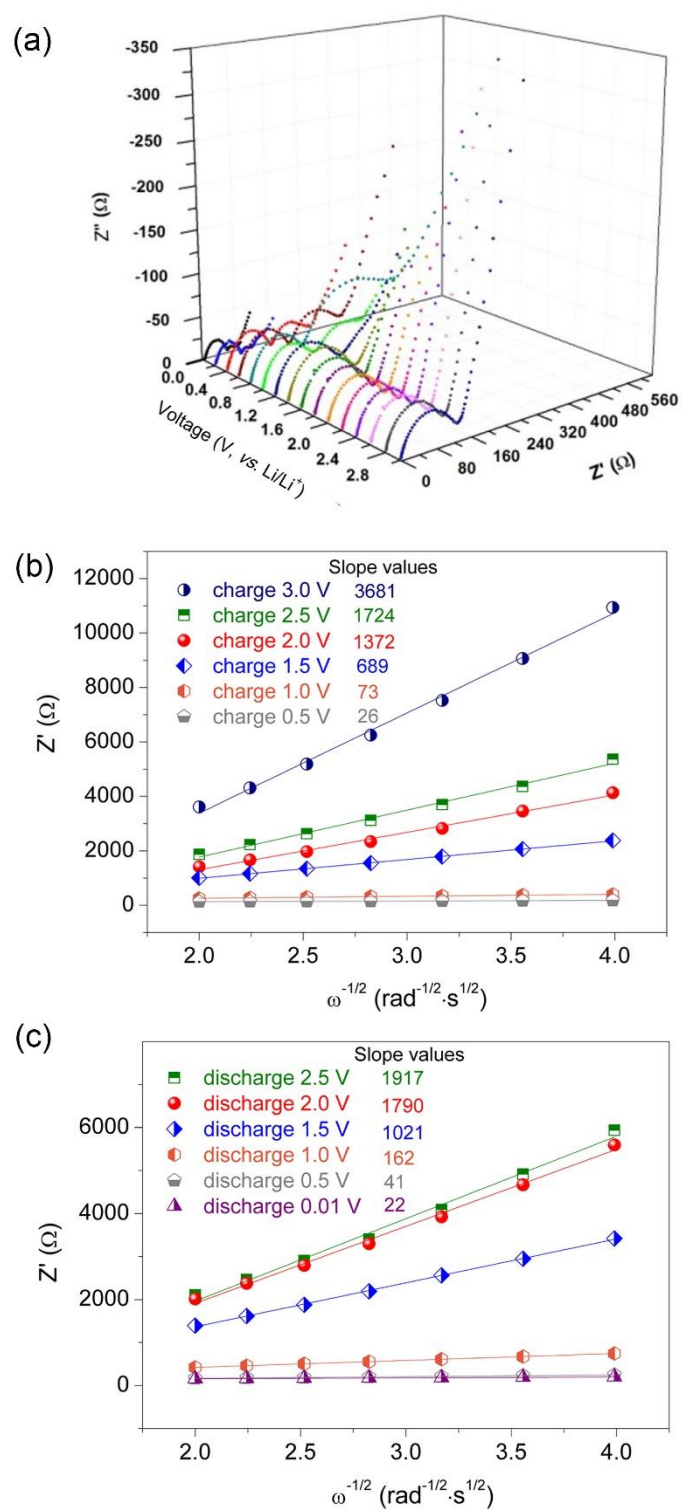


Figure S7. (a) EIS spectra of the charging process. The linear relationship between Z' and $\omega^{-1/2}$ in the (b) charge and (c) discharge process.

References

- 1 C. Liu, H. Song, C. Zhang, Y. Liu, C. Zhang, X. Nan and G. Cao, *Nano Res.*, 2015, **8**, 3372-3383.
- 2 G. Kresse and J. Furthmuller, *Comp. Mater. Sci.*, 1996, **6**, 15-50.
- 3 G. Kresse and D. Joubert, *Phys. Rev. B: Condens. Matter*, 1999, **59**, 1758-1775.
- 4 P. E. Blochl, *Phys. Rev. B: Condens. Matter*, 1994, **50**, 17953-17979.
- 5 J. P. Perdew, K. Burke and M. Ernzerhof, *Phys. Rev. Lett.*, 1996, **77**, 3865-3868.
- 6 K. Momma and F. Izumi, *J. Appl. Crystallogr.*, 2008, **41**, 653-658.
- 7 Y. Hao, C. Chen, X. Yang, G. Xiao, B. Zou, J. Yang and C. Wang, *J. Power Sources*, 2017, **338**, 9-16.
- 8 S.Y. Lee, K.Y. Park, W.S. Kim, S. Yoon, S.H. Hong, K. Kang and M. Kim, *Nano Energy*, 2016, **19**, 234-245.
- 9 L. Zhang, G. Xia, Y. Huang, C. Wei, Y. Yu, D. Sun and X. Yu, *Energy Storage Mater.*, 2018, **10**, 160-167.
- 10 L. Sheng, S. Liang, T. Wei, J. Chang, Z. Jiang, L. Zhang, Q. Zhou, J. Zhou, L. Jiang and Z. Fan, *Energy Storage Mater.*, 2018, **12**, 94-102.
- 11 D. Sun, Y. Tang, D. Ye, J. Yan, H. Zhou and H. Wang, *ACS Appl. Mater. Interfaces*, 2017, **9**, 5254-5262.
- 12 Z. Cao, M. Shi, Y. Ding, J. Zhang, Z. Wang, H. Dong, Y. Yin and S. Yang, *J. Phys. Chem. C*, 2017, **121**, 2546-2555.
- 13 X. Tang, G. Sui, Q. Cai, W. Zhong and X. Yang, *J. Mater. Chem. A*, 2016, **4**, 2082-2088
- 14 C. Liu, C. Zhang, H. Song, C. Zhang, Y. Liu, X. Nan and G. Cao, *Nano Energy*, 2016, **22**, 290-300.
- 15 C. Liu, C. Zhang, H. Song, X. Nan, H. Fu and G. Cao, *J. Mater. Chem. A*, 2016, **4**, 3362-3370.
- 16 X. Jiang, W. Yu, H. Wang, H. Xu, X. Liu and Y. Ding, *J. Mater. Chem. A*, 2016, **4**, 920-925.
- 17 B.K. Zou, Y.Y. Zhang, J.Y. Wang, X. Liang, X.H. Ma and C.H. Chen, *Electrochim. Acta*, 2015, **167**, 25-31.
- 18 F. Zheng, G. Xia, Y. Yang and Q. Chen, *Nanoscale*, 2015, **7**, 9637-9645.
- 19 J. G. Wang, C. B. Zhang, D. D. Jin, K. Y. Xie and B. Q. Wei, *J. Mater. Chem. A*, 2015, **3**, 13699-13705.
- 20 H. Park, D. Yeom, J. Kim and J. Lee, *Korean J. Chem. Eng.*, 2015, **32**, 178-183.
- 21 S. Zhang, L. Zhu, H. Song, X. Chen and J. Zhou, *Nano Energy*, 2014, **10**, 172-180.
- 22 Y. Xiao, X. Wang, W. Wang, D. Zhao and M. Cao, *ACS Appl. Mater. Interfaces*, 2014, **6**, 2051-2058.
- 23 S. Wang, Y. Ren, G. Liu, Y. Xing and S. Zhang, *Nanoscale*, 2014, **6**, 3508-3512.
- 24 H. L. Wang, Z. W. Xu, Z. Li, K. Cui, J. Ding, A. Kohandehghan, X. H. Tan, B. Zahiri, B. C. Olsen, C. M. B. Holt and D. Mitlin, *Nano Lett*, 2014, **14**, 1987-1994.
- 25 K. Su, C. Wang, H. G. Nie, Y. Guan, F. Liu and J. T. Chen, *J. Mater. Chem. A*, 2014, **2**, 10000-10006.
- 26 S. M. Guo, G. X. Lu, S. Qiu, J. R. Liu, X. Z. Wang, C. Z. He, H. G. Wei, X. R. Yan and Z. H. Guo, *Nano Energy*, 2014, **9**, 41-49.
- 27 Y. Xia, Z. Xiao, X. Dou, H. Huang, X. H. Lu, R. J. Yan, Y. P. Gan, W. J. Zhu, J. P. Tu, W. K. Zhang and X. Y. Tao, *ACS Nano*, 2013, **7**, 7083-7092.
- 28 W.M. Chen, L. Qie, Y. Shen, Y.M. Sun, L.X. Yuan, X.L. Hu, W.X. Zhang and Y.H. Huang, *Nano Energy*, 2013, **2**, 412-418.
- 29 B. Sun, Z. Chen, H.-S. Kim, H. Ahn and G. Wang, *J. Power Sources*, 2011, **196**, 3346-3349.